

# Identifying Finite-Time Coherent Sets from Limited Quantities of Lagrangian Data

Matthew O. Williams,<sup>1</sup> Irina I. Rypina,<sup>2</sup> and Clarence W. Rowley<sup>3</sup>

<sup>1</sup>*Program in Applied and Computational Mathematics, Princeton University, NJ 08544.*

<sup>2</sup>*Department of Physical Oceanography, Woods Hole Oceanographic Institute, MA 02543.*

<sup>3</sup>*Department of Mechanical and Aerospace Engineering, Princeton University, NJ 08544.*

A data-driven procedure for identifying the dominant transport barriers in a time-varying flow from limited quantities of Lagrangian data is presented. Our approach partitions state space into pairs of coherent sets, which are sets of initial conditions chosen to minimize the number of trajectories that “leak” from one set to the other under the influence of a stochastic flow field during a pre-specified interval in time. In practice, this partition is computed by posing an optimization problem, which once solved, yields a pair of functions whose signs determine set membership. From prior experience with synthetic, “data rich” test problems and conceptually related methods based on approximations of the Perron-Frobenius operator, we observe that the functions of interest typically appear to be smooth. As a result, given a fixed amount of data our approach, which can use sets of globally supported basis functions, has the potential to more accurately approximate the desired functions than other functions tailored to use compactly supported indicator functions. This difference enables our approach to produce effective approximations of pairs of coherent sets in problems with relatively limited quantities of Lagrangian data, which is usually the case with real geophysical data. We apply this method to three examples of increasing complexity: the first is the double gyre, the second is the Bickley Jet, and the third is data from numerically simulated drifters in the Sulu Sea.

Transport barriers separate a fluid flow into regions with qualitatively different Lagrangian behavior, and are important for understanding transport and stirring processes in geophysical flows. We present a method for identifying these barriers by partitioning the state space of the system into coherent sets that are chosen to minimize the number of trajectories that “switch” sets in a given time interval. There are many conceptual similarities between our approach and probabilistic methods, but our approach is tailored to problems with limited quantities of Lagrangian data, which is often the case when the data come from real instruments such as “drifters” released into the ocean. In particular, we exploit the apparent smoothness of the globally supported basis functions used to define these sets, which lead to a faster convergence compared to the more commonly used choices such as indicator functions. As a result, useful (although not fully converged) approximations of the coherent sets can be obtained from fewer Lagrangian trajectories compared to other methods. This approach is applied to identify coherent sets in three fluid flows: the double gyre, which is commonly used as a benchmark for different methods, the Bickley Jet, which is an idealized model for stratospheric flow, and the third is a realistic numerically generated near-surface flow in the Sulu Sea, where the method successfully identifies coherent sets from limited numbers of numerically simulated drifters.

## I. INTRODUCTION

The identification of transport barriers is an important step in understanding fluid flows that have complex and often chaotic dynamics. The locations (or absence) of these barriers helps to determine the mixing properties of the underlying flow<sup>1–3</sup>, and have practical applications in a number of engineering contexts including chemical reactors and combustion<sup>1</sup> as well as ecological applications, such as predicting the extent of oil spills<sup>4,5</sup>. The primary difficulty in these settings is identifying the dominant barriers to transport, and a number of effective yet conceptually different methods have been developed to do so. Geometric methods focus on the identification of invariant manifolds and finite-time hyperbolic material lines<sup>6,7</sup>, and include methods based on Finite Time or Finite Scale Lyapunov Exponents<sup>8–10</sup> and the associated Lagrangian Coherent Structures<sup>11–13</sup>, which are perhaps the most widely used approaches at the current time. However, there are alternative techniques including variational methods<sup>14</sup>, ergodic quotient partitions<sup>15</sup>, trajectory complexity measures<sup>12</sup> and Lagrangian descriptors<sup>16</sup>.

In recent years, probabilistic methods, which use a different definition of coherence, have proved to be a useful alternative to geometric methods<sup>17–21</sup>, and though they have been applied to general flows, have the advantage of identifying minimally dispersive regions when the flow happens to be autonomous or time-periodic<sup>22</sup>. Many probabilistic approaches define coherent sets based on the spectral properties of the Perron-Frobenius operator (which is also referred to as the transfer operator)<sup>17–21</sup>.

In practice, this information is often obtained by constructing a finite-dimensional approximation of this operator using the Ulam-Galerkin method<sup>17,18,21,23</sup>, which has been implemented efficiently in software packages such as GAIO<sup>23</sup>.

Many of these methods also assume that the velocity field that defines the motion of fluid parcels or drifters is available. In problems where these velocities are unknown, they can often be approximated using optical flow and other data driven methods<sup>24,25</sup>. Although these approaches could, in principle, be applied directly to Lagrangian data, the amount of data required for an accurate approximation is often too large to be practical in an experimental setting. Our ambition in this manuscript is to demonstrate that effective approximations of coherent sets can be obtained with limited quantities of Lagrangian data, and is therefore well suited to experimentally obtained data sets.

We compute coherent sets by solving an optimization problem, which once suitably relaxed, can be accomplished using the Singular Value Decomposition. The result is a pair of functions whose signs can be used to partition the data into two sets chosen to minimize the number of elements that “leak out” in a given time interval. In the limit of infinite data, this problem can be succinctly expressed as an inner product involving the Koopman operator<sup>26–29</sup>, and is conceptually similar to the analytical definition presented by Froyland<sup>20</sup>. The method presented here should be thought of as a different finite-dimensional approximation of this overarching problem, and similar to the algorithms implemented in GAIO that approximate the Perron-Frobenius operator using indicator functions<sup>23</sup>.

Unlike those methods, our approach allows more freedom in the choice of basis functions; in particular, it enables globally supported functions to be used. From “data rich” examples and pre-existing efforts using transfer operator methods<sup>18,21,22,30</sup>, we have observed that the functions of interest often appear to be smooth, and therefore, globally supported basis functions have the potential to converge more rapidly to the solution than compactly supported ones such as indicator functions. Intuitively, the differences between our approach and GAIO are analogous to the differences between spectral methods<sup>31,32</sup> and finite-volume methods<sup>33</sup>; while both approaches can be equally accurate, spectral methods typically approximate a linear operator using a small number of globally supported basis functions, while finite volume methods use a larger but compactly supported set. In practice, this more rapid convergence enables “effective” approximations to be obtained with fewer basis functions, and hence, fewer data points, which makes our approach well suited for the “data poor” regime that often occurs experimentally.

The remainder of the manuscript is outlined as follows: in Sec. II we give a definition of a coherent set in terms of a solution to a data-driven optimization problem. In Sec. III, we consider the infinite data limit, where this

problem can be recast into one involving the Koopman operator. As a result, methods like Generalized Laplace Analysis<sup>28,29,34</sup> or Extended Dynamic Mode Decomposition (Extended DMD)<sup>35</sup>, could be “re-tasked” to compute coherent sets. Furthermore, this limit makes the connection between our approach and the analytical definition presented by Froyland<sup>20</sup> more clear. In Sec. IV, we apply our method to three examples: the double gyre, the Bickley Jet, and numerically simulated drifters in the Sulu Sea, in order to demonstrate that the approach is effective in practice. Finally in Sec. V, we present some brief concluding remarks.

## II. A DEFINITION OF COHERENT SETS

In this section, we construct the optimization problem whose solution defines our pairs of coherent sets. As we will demonstrate in Sec. III, this approach is conceptually equivalent to the one presented analytically by Froyland<sup>20</sup> and implemented using packages like GAIO<sup>23</sup>. As a result, there are many similarities between what was done in Refs. 17–19 and what we do here; indeed, the manipulations that follow are motivated by those references and Ref. 20. The key difference is that those approaches are tailored to use compactly supported functions such as indicator functions, while our approach is compatible with any reasonable basis set that includes the constant function. This is advantageous because globally supported basis functions can often produce more accurate approximations of the functions that define the coherent set pairs than indicator functions given a limited amount of data, which is often the case in experiments where the data are generated by drifters.

We assume we are given a collection of  $M$  drifters, whose evolution is completely determined by the velocity field of some underlying flow, that are initially contained in some domain,  $\Omega_X \subseteq \Omega$ , at time  $n$ , but migrate to another domain,  $\Omega_Y \subseteq \Omega$ , at time  $n + 1$ . These pairs of positions are collected into the set  $\{(\mathbf{x}_m, \mathbf{y}_m)\}_{m=1}^M$  where  $\mathbf{x}_m$  is the position of the  $m$ -th drifter at time  $n$ , and  $\mathbf{y}_m$  is the position of that drifter at time  $n + 1$ . Our objective is to partition these drifters into two sets –  $X_1$  and  $X_2$  at time  $n$  and  $Y_1$  and  $Y_2$  at time  $n + 1$  – based on their *physical positions* at times  $n$  and  $n + 1$  respectively. To do this we define a pair of functions,  $f_X : \Omega_X \rightarrow \pm 1$  and  $f_Y : \Omega_Y \rightarrow \pm 1$ ; at time  $n$ , the sign of  $f_X$  determines whether a point is in  $X_1$  or  $X_2$ , and at time  $n + 1$ , the sign of  $f_Y$  is used to assign the data points to either  $Y_1$  or  $Y_2$ .

In principle, the problem specified above is not enough to uniquely partition the data even in the infinite data limit. As shown in Ref. 20, the functions  $f_X$  and  $f_Y$  will only identify useful coherent sets if the flow that maps  $\mathbf{x}_m$  to  $\mathbf{y}_m$  is stochastic. When this mapping is deterministic, one can find a pair of functions such that  $g(f_X, f_Y) = 1$  for any admissible partition of  $\Omega_X$  and  $\Omega_Y$  simply by choosing  $Y_1$  to be the image of the set  $X_1$ , and defining

$f_X$  and  $f_Y$  appropriately. To produce a pair of *distinct* coherent sets, some stochasticity is required, and when this is not introduced naturally by the underlying flow, we *make the system stochastic* by explicitly injecting “noise” into our data by perturbing the  $\mathbf{y}_m$ , which makes it appear like a single  $\mathbf{x}_m$  has multiple images<sup>20</sup>. Because this is, in effect, changing the underlying flow, the choice of noise will impact the numerically computed coherent sets. However, we expect the sets to be qualitatively similar for any reasonably chosen noise, and in practice, the functions and data used to approximate  $f_X$  and  $f_Y$  often have a larger impact on the results than the noise term.

Intuitively, a *useful* pair of coherent sets should consist of two sets with elements that do not “leak” from one set to the other over a finite interval in time. In our framework, achieving this intuitive goal is equivalent to minimizing the number of drifters that switch sets, or equivalently, the number of points where  $f_X(\mathbf{x}_m) \leq 0$  but  $f_Y(\mathbf{y}_m) > 0$  (and *vice versa*). More concretely, we maximize the following function:

$$g(f_X, f_Y) = \frac{1}{M} \sum_{m=1}^M f_X(\mathbf{x}_m) f_Y(\mathbf{y}_m), \quad (1)$$

which attains its maximum value of 1 if no drifters “switch sets.”

Without additional constraints, a global maximum can be obtained trivially by assigning *all* the data points to one set or the other. To force the algorithm to partition the data into two *nonempty sets*, we include another pair of constraints that specify the relative sizes of  $X_1$  and  $X_2$  and  $Y_1$  and  $Y_2$ . In particular, we require that:

$$\frac{1}{M} \sum_{m=1}^M f_X(\mathbf{x}_m) = \varepsilon_X, \quad \frac{1}{M} \sum_{m=1}^M f_Y(\mathbf{y}_m) = \varepsilon_Y, \quad (2)$$

where  $\varepsilon_X$  and  $\varepsilon_Y$  are two constants that determine the difference in the number of elements in  $X_1$  and  $X_2$  and  $Y_1$  and  $Y_2$  respectively. To obtain two sets of equal size, we set  $\varepsilon_X = \varepsilon_Y = 0$ . However, it is often advantageous to allow the  $\varepsilon$  to vary as not all systems can be (or should be) decomposed into two sets of equal size.

In combination, this results in the following constrained optimization problem:

$$\max_{f_X, f_Y} g(f_X, f_Y) \quad (3a)$$

$$\text{subject to: } \frac{1}{M} \sum_{m=1}^M f_X(\mathbf{x}_m) = \varepsilon_X \quad (3b)$$

$$\frac{1}{M} \sum_{m=1}^M f_Y(\mathbf{y}_m) = \varepsilon_Y, \quad (3c)$$

whose solutions we would like to approximate. However, there are two immediately obvious issues that make (3) difficult to solve: (i) we are maximizing  $g$  over an infinite dimensional space ( $f_X$  and  $f_Y$  are functions), and

(ii)  $f_X : \Omega_X \rightarrow \pm 1$  and  $f_Y : \Omega_Y \rightarrow \pm 1$  rather than real numbers. Therefore, even a finite dimensional approximation of  $f_X$  and  $f_Y$  would result in a zero-one quadratic program<sup>36</sup>, which is computationally expensive to solve.

### A. A Finite Dimensional Approximation

The “conceptual” optimization problem in (3) is intuitively useful, but too difficult to solve in practice. We compute an approximate solution by: (i) relaxing the constraint that  $f_X : \Omega_X \rightarrow \pm 1$  and  $f_Y : \Omega_Y \rightarrow \pm 1$  and allowing  $f_X : \Omega_X \rightarrow \mathbb{R}$  and  $f_Y : \Omega_Y \rightarrow \mathbb{R}$ , and (ii) approximating  $f_X$  and  $f_Y$  with functions that lie in the subspace spanned by two sets of basis functions that we denote as  $\{\psi_k\}_{k=1}^{K_X}$  and  $\{\tilde{\psi}_k\}_{k=1}^{K_Y}$  for  $f_X$  and  $f_Y$  respectively. In order to guarantee the resulting optimization problem can be easily solved regardless of the choice of  $\psi_k$  and  $\tilde{\psi}_k$ , we require that the first elements in each set are the relevant constant functions,  $\psi_1(\mathbf{x}) = 1$  and  $\tilde{\psi}_1(\mathbf{y}) = 1$ . This constraint is not a necessary condition for our approach, and some basis sets (e.g., indicator functions) violate this constraint and still produce useful results. Next, we define the vector-valued functions,

$$\boldsymbol{\psi}_X(\mathbf{x}) = \begin{bmatrix} \psi_1(\mathbf{x}) \\ \psi_2(\mathbf{x}) \\ \vdots \\ \psi_{K_X}(\mathbf{x}) \end{bmatrix}, \quad \boldsymbol{\psi}_Y(\mathbf{y}) = \begin{bmatrix} \tilde{\psi}_1(\mathbf{y}) \\ \tilde{\psi}_2(\mathbf{y}) \\ \vdots \\ \tilde{\psi}_{K_Y}(\mathbf{y}) \end{bmatrix}. \quad (4)$$

Then, our finite-dimensional approximations of  $f_X$  and  $f_Y$  are simply

$$f_X = \sum_{k=1}^{K_X} a_k \psi_k = \boldsymbol{\psi}_X^T \mathbf{a}, \quad f_Y = \sum_{k=1}^{K_Y} \tilde{a}_k \tilde{\psi}_k = \boldsymbol{\psi}_Y^T \tilde{\mathbf{a}}, \quad (5)$$

for some appropriate vector of coefficients  $\mathbf{a}$  and  $\tilde{\mathbf{a}}$ . Because the maximum values of  $f_X$  and  $f_Y$  are no longer bounded, we include two additional constraints:

$$\frac{1}{M} \sum_{m=1}^M |f_X(\mathbf{x}_m)|^2 = \frac{1}{M} \sum_{m=1}^M |f_Y(\mathbf{y}_m)|^2 = 1, \quad (6)$$

that impose an overall scaling on both functions.

With this approximation, the objective function can be written as:

$$g(f_X, f_Y) = \mathbf{a}^T \left( \frac{1}{M} \sum_{m=1}^M \boldsymbol{\psi}_X(\mathbf{x}_m) \boldsymbol{\psi}_Y^T(\mathbf{y}_m) \right) \tilde{\mathbf{a}} = \mathbf{a}^T \mathbf{A} \tilde{\mathbf{a}}. \quad (7)$$

Similarly, the constraints, (3b,c) and (6), can be written

as:

$$\frac{1}{M} \sum_{m=1}^M \psi_1(\mathbf{x}_m) f_X(\mathbf{x}_m) = \mathbf{e}_1^T \mathbf{G}_X \mathbf{a} = \varepsilon_X, \quad (8a)$$

$$\frac{1}{M} \sum_{m=1}^M \tilde{\psi}_1(\mathbf{y}_m) f_Y(\mathbf{y}_m) = \tilde{\mathbf{e}}_1^T \mathbf{G}_Y \tilde{\mathbf{a}} = \varepsilon_Y, \quad (8b)$$

$$\frac{1}{M} \sum_{m=1}^M f_X(\mathbf{x}_m) f_X(\mathbf{x}_m) = \mathbf{a}^T \mathbf{G}_X \mathbf{a} = 1, \quad (8c)$$

$$\frac{1}{M} \sum_{m=1}^M f_Y(\mathbf{y}_m) f_Y(\mathbf{y}_m) = \tilde{\mathbf{a}}^T \mathbf{G}_Y \tilde{\mathbf{a}} = 1, \quad (8d)$$

which make frequent use of the choice of  $\psi_1 = 1$  and  $\tilde{\psi}_1 = 1$ . Here  $\mathbf{e}_1$  and  $\tilde{\mathbf{e}}_1$  are the first unit vectors in  $\mathbb{R}^{K_X}$  and  $\mathbb{R}^{K_Y}$  respectively, and

$$\mathbf{G}_X \triangleq \frac{1}{M} \sum_{m=1}^M \psi(\mathbf{x}_m) \psi(\mathbf{x}_m)^T, \quad (9a)$$

$$\mathbf{G}_Y \triangleq \frac{1}{M} \sum_{m=1}^M \tilde{\psi}(\mathbf{y}_m) \tilde{\psi}(\mathbf{y}_m)^T, \quad (9b)$$

$$\mathbf{A} \triangleq \frac{1}{M} \sum_{m=1}^M \psi(\mathbf{x}_m) \tilde{\psi}(\mathbf{y}_m)^T. \quad (9c)$$

With this notation, the relaxed, finite-dimensional optimization problem is:

$$\max_{\mathbf{a}, \tilde{\mathbf{a}}} \mathbf{a}^T \mathbf{A} \tilde{\mathbf{a}} \quad (10a)$$

$$\text{subject to: } \mathbf{e}_1^T \mathbf{G}_X \mathbf{a} = \varepsilon_X, \quad (10b)$$

$$\tilde{\mathbf{e}}_1^T \mathbf{G}_Y \tilde{\mathbf{a}} = \varepsilon_Y, \quad (10c)$$

$$\mathbf{a}^T \mathbf{G}_X \mathbf{a} = \tilde{\mathbf{a}}^T \mathbf{G}_Y \tilde{\mathbf{a}} = 1. \quad (10d)$$

In summary, the objective function is  $\mathbf{a}^T \mathbf{A} \tilde{\mathbf{a}} = \sum_{m=1}^M f_X(\mathbf{x}_m) f_Y(\mathbf{y}_m)$ , and obtains its maximum value when  $f_X$  and  $f_Y$  have the same sign for every snapshot pair, which implies that we have “consistently” classified as many of the  $M$  data points as possible. The next two constraints determine the relative sizes of the sets, and are required to prevent the algorithm from assigning *all* the data to one set or the other. The final pair of constraints imposes a scaling on  $f_X$  and  $f_Y$ ; since our partition is based on the sign of these functions, any overall scaling will produce equivalent results. A schematic of this problem is given in Fig. 1. This optimization problem can be recast as a quadratically-constrained quadratic program for which solvers exist<sup>37</sup>, but are, once again, computationally expensive to use. In the next section, we will show that the solution can be obtained using the Singular Value Decomposition (SVD) if we transform the problem appropriately.

## B. Computing Coherent Sets in Practice

In this section, we will show that (10) can be solved using the SVD. The motivation for what follows is more mathematical than physical, and is inspired by the results of Froyland<sup>20</sup>. Specifically we note that:

1. The pair of vectors,  $\mathbf{u}$  and  $\mathbf{v}$ , that maximize the quantity  $\mathbf{u}^T \mathbf{A} \mathbf{v}$  are the left and right singular vectors of  $\mathbf{A}$  with the largest singular value, which we refer to as  $\mathbf{u}_1$  and  $\mathbf{v}_1$ .
2. If we add the constraints  $\mathbf{u}_1^T \mathbf{u} = \varepsilon_X$  and  $\mathbf{v}_1^T \mathbf{v} = \varepsilon_Y$ , then the optimal  $\mathbf{u}$  and  $\mathbf{v}$  become  $\mathbf{u} = \varepsilon_X \mathbf{u}_1 + c_u \mathbf{u}_2$  and  $\mathbf{v} = \varepsilon_Y \mathbf{v}_1 + c_v \mathbf{v}_2$  for some coefficients  $c_u$  and  $c_v$  where  $\mathbf{u}_2$  and  $\mathbf{v}_2$  are the singular vectors associated with the second largest singular value,  $\sigma_2$ .
3. If we add the scaling constraint  $\mathbf{u}^T \mathbf{u} = \mathbf{v}^T \mathbf{v} = 1$ , this imposes that  $c_u = \sqrt{1 - \varepsilon_X^2}$  and  $c_v = \sqrt{1 - \varepsilon_Y^2}$ , but does not change the form of the solution.

The main difference between this problem, which can be solved using the SVD, and (10) is that the constraints could be written in terms of the standard Euclidean inner product while (10) has constraints that are written in terms of weighted inner products.

Therefore, the first step is to transform our coordinates such that the constraints in (10) can be expressed in terms of “unweighted” inner products like in our model problem. To do this, we use the Cholesky Decomposition and let

$$\mathbf{G}_X = \mathbf{L}_X \mathbf{L}_X^T, \quad \mathbf{G}_Y = \mathbf{L}_Y \mathbf{L}_Y^T. \quad (11)$$

If we define  $\mathbf{b} = \mathbf{L}_X^T \mathbf{a}$  and  $\tilde{\mathbf{b}} = \mathbf{L}_Y^T \tilde{\mathbf{a}}$ , then the constraint equations simplify to

$$\mathbf{e}_1^T \mathbf{b} = \varepsilon_X, \quad (12a)$$

$$\tilde{\mathbf{e}}_1^T \tilde{\mathbf{b}} = \varepsilon_Y, \quad (12b)$$

$$\mathbf{b}^T \mathbf{b} = \tilde{\mathbf{b}}^T \tilde{\mathbf{b}} = 1, \quad (12c)$$

where  $\varepsilon_X = \varepsilon_X / \mathbf{L}_X^{(11)}$ ,  $\varepsilon_Y = \varepsilon_Y / \mathbf{L}_Y^{(11)}$ ,  $\mathbf{L}_X^{(11)} \in \mathbb{R}$  denotes the element in the first row and column of  $\mathbf{L}_X$ . These terms appear because  $\mathbf{L}_X$  (or  $\mathbf{L}_Y$ ) is lower-triangular, and therefore  $\mathbf{e}_1^T \mathbf{L}_X = \mathbf{L}_X^{(11)} \mathbf{e}_1^T$ . We also rewrite the objective function, and set  $\mathbf{a}^T \mathbf{A} \tilde{\mathbf{a}} = \mathbf{b}^T \hat{\mathbf{A}} \tilde{\mathbf{b}}$  where

$$\hat{\mathbf{A}} \triangleq \mathbf{L}_X^{-1} \mathbf{A} \mathbf{L}_Y^{-T}. \quad (13)$$

This results in a transformed system of equations

$$\max_{\mathbf{b}, \tilde{\mathbf{b}}} \mathbf{b}^T \hat{\mathbf{A}} \tilde{\mathbf{b}}, \quad (14a)$$

$$\text{subject to: } \mathbf{e}_1^T \mathbf{b} = \varepsilon_X, \quad (14b)$$

$$\tilde{\mathbf{e}}_1^T \tilde{\mathbf{b}} = \varepsilon_Y, \quad (14c)$$

$$\mathbf{b}^T \mathbf{b} = \tilde{\mathbf{b}}^T \tilde{\mathbf{b}} = 1, \quad (14d)$$

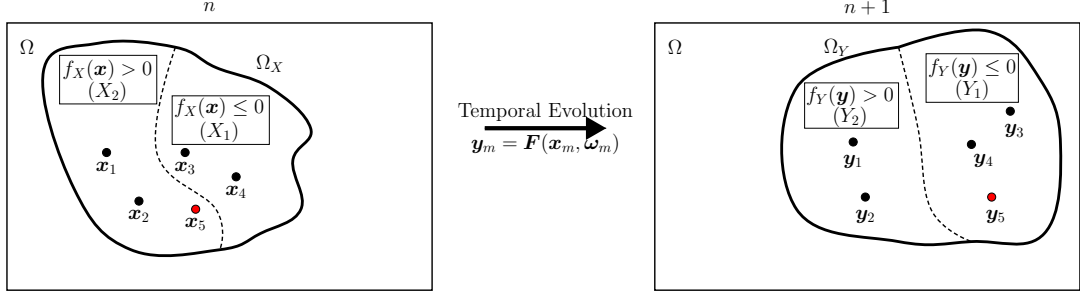


Figure 1. A “cartoon” of the coherent set definition in this manuscript. Given data from a discrete time dynamical system whose evolution operator at time  $n$  is  $\mathbf{F}$ , where  $\omega_m$  represents the “noise” added to the system, our objective is to identify two functions,  $f_X : \Omega_X \rightarrow \mathbb{R}$  and  $f_Y : \Omega_Y \rightarrow \mathbb{R}$ , whose signs will be used to partition  $\Omega_X$  and  $\Omega_Y$  into  $X_1$  and  $X_2$  or  $Y_1$  and  $Y_2$  respectively. These functions are determined by solving the optimization problem in (10). Intuitively, the computed functions minimize the number of “mis-classified” points, such as  $\mathbf{x}_5$ , that are assigned to the two different sets,  $X_1$  or  $X_2$  and  $Y_1$  or  $Y_2$ , at times  $n$  and  $n+1$ . In general,  $\Omega_Y \neq \Omega_X$ , so the basis functions used to approximate  $f_X$  and  $f_Y$  could (and typically should) differ.

which is formally equivalent to our model problem because  $\mathbf{e}_1$  and  $\tilde{\mathbf{e}}_1$  are the left and right singular vectors of  $\hat{\mathbf{A}}$  with  $\sigma_1 = 1$ . It is simple, but tedious, to show this, and a proof based on the block structure of  $\hat{\mathbf{A}}$  is given in Appendix A.

Therefore, the solution to (14) is of the form:

$$\mathbf{b} = \hat{\varepsilon}_X \mathbf{e}_1 + \sqrt{1 - \hat{\varepsilon}_X^2} \mathbf{u}_2, \quad (15a)$$

$$\tilde{\mathbf{b}} = \hat{\varepsilon}_Y \tilde{\mathbf{e}}_1 + \sqrt{1 - \hat{\varepsilon}_Y^2} \mathbf{v}_2, \quad (15b)$$

where  $\mathbf{u}_2$  and  $\mathbf{v}_2$  are the left and right singular vectors associated with  $\sigma_2$ , the largest singular value not equal to  $\sigma_1 = 1$ . In what follows, we will assume that  $\sigma_2 < \sigma_1 = 1$ . Because this is not necessarily true for all combinations of basis functions and data, we treat this condition as a “sanity check” on the procedure. If  $\sigma_2 > 1$ , then the computation is most likely unreliable.

Once  $\mathbf{b}$  and  $\tilde{\mathbf{b}}$  have been computed, we let  $\mathbf{a} = \mathbf{L}_X^{-T} \mathbf{b}$  and  $\tilde{\mathbf{a}} = \mathbf{L}_Y^{-T} \tilde{\mathbf{b}}$ , and approximate  $f_X$  and  $f_Y$  at any desired points using (5). The final step in the procedure is partition  $\Omega_X$  and  $\Omega_Y$  using the numerically computed  $f_X$  and  $f_Y$ . We define

$$X_1 = \{\mathbf{x} \in \Omega_X : f_X(\mathbf{x}) \leq 0\}, \quad (16a)$$

$$Y_1 = \{\mathbf{y} \in \Omega_Y : f_Y(\mathbf{y}) \leq 0\}, \quad (16b)$$

and let  $X_2$  and  $Y_2$  be their complements (or, equivalently, the subset where  $f_X, f_Y > 0$ ). The values of  $\varepsilon_X$  and  $\varepsilon_Y$  effectively add a constant offset to both  $f_X$  and  $f_Y$ . As a result,  $\varepsilon_X$  and  $\varepsilon_Y$  can be determined “after the fact,” and following Ref. 19, we will choose them so that the computed  $f_X$  and  $f_Y$  maximize the fraction of “consistently classified points” (i.e., if  $\mathbf{x}_m \in X_1$  then  $\mathbf{y}_m \in Y_1$ ) in the pairs of sets  $(X_1, Y_1)$  and  $(X_2, Y_2)$ . Although we do not place any explicit constraints on the  $\varepsilon$ , we typically require that neither  $\varepsilon_X$  nor  $\varepsilon_Y$  can be so large or small that either  $X_1$  or  $X_2$  (or  $Y_1$  and  $Y_2$ ) contain a “negligible” number of data points.

### C. Algorithm Summary

In practice, this algorithm requires the user to provide three quantities: (i) a data set of snapshot pairs,  $\{(\mathbf{x}_m, \mathbf{y}_m)\}_{m=1}^M$ , (ii) two sets of basis functions that comprise the vector-valued functions  $\boldsymbol{\psi}_X$  and  $\boldsymbol{\psi}_Y$ , and (iii) the “noise” that will be added to the data. The first two quantities are important if this method is to perform well, but because they are highly problem dependent, we will defer the discussion of these choices until Sec. IV where we apply the method to our example problems. The addition of noise will, in principle, affect the resulting sets, but in practice, appears to have a smaller impact than the data and basis functions provided the noise chosen is not too large. Given these quantities, the coherent sets are computed as follows:

1. Augment the existing data set with noise by “looping” through the data multiple times and applying randomly generated perturbations to  $\mathbf{y}_m$ . The perturbed data pairs, e.g.,  $(\mathbf{x}_m, \mathbf{y}_m + \delta \mathbf{y}_m)$ , are added to the existing set of data, and will be used in the steps that follow. The choice of noise and the number of iterates typically has only a small impact on the resulting coherent sets, and this step, while necessary conceptually, can often be ignored in practice.
2. Compute the matrices in (9), their Cholesky decomposition in (11), and the matrix  $\hat{\mathbf{A}}$  in (13).
3. Using the SVD, let  $\hat{\mathbf{A}} = \mathbf{U} \boldsymbol{\Sigma} \mathbf{V}^T$ .
4. As a sanity check, examine  $\sigma_2$ , which is the largest singular value that is not unity. If  $\sigma_2 > 1$ , this computation is “over-fitting” the data, and is unlikely to produce a useful pair of coherent sets. In our experience, reducing the number of basis functions will correct this problem. In practice, we it-

erate through steps 2-4, and select the largest basis where  $\sigma_2 < 1$ .

5. Choose values of  $\varepsilon_X$  and  $\varepsilon_Y$ , and compute  $\mathbf{b}$  and  $\tilde{\mathbf{b}}$  using (15). To obtain sets with less “leakage”, we choose these values to minimize the fraction of misclassified points, which is similar to the concept of *coherence* in Refs. 18,19. In practice, simply letting  $\varepsilon_X = \varepsilon_Y = 0$  is sufficient in many applications.
6. Compute  $\mathbf{a} = \mathbf{L}_X^{-T} \mathbf{b}$  and  $\tilde{\mathbf{a}} = \mathbf{L}_Y^{-T} \tilde{\mathbf{b}}$ , which are the solutions of the original relaxed, finite-dimensional optimization problem.
7. Finally, compute the value of  $f_X$  or  $f_Y$  at any desired points using (5), and partition the domain based on the sign of  $f_X$ .

This algorithm runs in  $\mathcal{O}(K^2 \max(K, M))$  time, where  $K = \max(K_X, K_Y)$ . The asymptotic cost is determined either by the need to assemble  $\mathbf{G}_X$ ,  $\mathbf{G}_Y$  and  $\mathbf{A}$ , which is an  $\mathcal{O}(K^2 M)$  computation, or in constructing and decomposing  $\hat{\mathbf{A}}$  which is  $\mathcal{O}(K^3)$  due to matrix inversion and singular vector computations. In principle, the computation of  $\mathbf{G}_X$ ,  $\mathbf{G}_Y$ , and  $\mathbf{A}$  could be easily accomplished in parallel, but in our current serial code, obtaining these matrices is the most time-consuming step.

If more than two coherent sets are desired, we repeat the procedure outlined above in a recursive fashion using the data in  $X_1$  and  $Y_1$  and the data in  $X_2$  and  $Y_2$  separately. Similar to the work of Ma and Bollt<sup>30</sup>, this results in a larger number of coherent sets that can capture finer spatial features. In practice, we terminate this iteration procedure if more than 5% of the data in any pair of sets “leaks out” during the interval of interest so that all of the resulting sets will, visually, appear to be coherent.

### III. CONNECTIONS TO THE KOOPMAN OPERATOR

The algorithm presented in Sec. II is both conceptually and mathematically related to the approach presented in Refs. 18–20; indeed, the primary difference between the approaches is that we can use a “richer” set of basis functions to represent  $f_X$  and  $f_Y$ . In this section, we examine the “infinite data” limit, which is the limit where our approach can be compared to these transfer operator-based methods.

In all that follows, we assume our data set  $\{(\mathbf{x}_m, \mathbf{y}_m)\}_{m=1}^M$  is constructed by randomly choosing initial conditions,  $\mathbf{x}_m$ , from a (spatial) distribution  $\rho$ . As before,  $\mathbf{y}_m$  is the location of the  $m$ -th drifter at time  $n+1$ , and  $\nu$  is the new spatial distribution of the drifters. If the evolution operator from time  $n$  to  $n+1$  is  $\mathbf{F}$ , then  $\mathbf{y}_m = \mathbf{F}(\mathbf{x}_m, \boldsymbol{\omega}_m)$  where  $\boldsymbol{\omega}_m$  accounts for the noise that is artificially added to the flow map or the stochasticity naturally in the flow.

In the limit as  $M \rightarrow \infty$ , the  $ij$ -th element of  $\mathbf{G}_X$  is almost surely:

$$\lim_{M \rightarrow \infty} \mathbf{G}_X^{(ij)} = \lim_{M \rightarrow \infty} \frac{1}{M} \sum_{m=1}^M \psi_i(\mathbf{x}_m) \psi_j(\mathbf{x}_m) = \langle \psi_i, \psi_j \rangle_\rho, \quad (17)$$

where  $\langle f, g \rangle_\rho = \int_{\Omega_X} f(\mathbf{x}) g(\mathbf{x}) \rho(\mathbf{x}) d\mathbf{x}$ . This argument follows directly from the law of large numbers, and the stochastic manner in which new initial conditions are added. Similarly,

$$\lim_{M \rightarrow \infty} \mathbf{G}_Y^{(ij)} = \lim_{M \rightarrow \infty} \frac{1}{M} \sum_{m=1}^M \tilde{\psi}_i(\mathbf{y}_m) \tilde{\psi}_j(\mathbf{y}_m) = \langle \tilde{\psi}_i, \tilde{\psi}_j \rangle_\nu, \quad (18)$$

where  $\langle f, g \rangle_\nu = \int_{\Omega_Y} f(\mathbf{y}) g(\mathbf{y}) \nu(\mathbf{y}) d\mathbf{y}$ . In this limit, both  $\mathbf{G}_X$  and  $\mathbf{G}_Y$  are Gram matrices where each element is an inner product between basis functions weighted by the density of the data.

Unlike  $\mathbf{G}_X$  and  $\mathbf{G}_Y$ , the  $ij$ -th element of  $\mathbf{A}$  depends upon both the randomly selected initial conditions,  $\mathbf{x}_m$ , and their images,  $\mathbf{y}_m$ , which are affected by the stochasticity in the dynamics. Assuming that the  $\mathbf{x}_m$  and  $\boldsymbol{\omega}_m$  are chosen independently,

$$\begin{aligned} \lim_{M \rightarrow \infty} \mathbf{A}^{(ij)} &= \lim_{M \rightarrow \infty} \frac{1}{M} \sum_{m=1}^M \psi_i(\mathbf{x}_m) \tilde{\psi}_j(\mathbf{y}_m) \\ &= \lim_{M \rightarrow \infty} \frac{1}{M} \sum_{m=1}^M \psi_i(\mathbf{x}_m) \tilde{\psi}_j(\mathbf{F}(\mathbf{x}_m, \boldsymbol{\omega}_m)) \\ &= \int_{\Omega_X} \mathbb{E}[\psi_i(\mathbf{x}) \tilde{\psi}_j(\mathbf{F}(\mathbf{x})) \rho(\mathbf{x})] d\mathbf{x} \\ &= \langle \psi_i, \mathbb{E}[\tilde{\psi}_j \circ \mathbf{F}] \rangle_\rho, \end{aligned} \quad (19)$$

where  $\mathbb{E}$  denotes the expected value over the stochasticity in the dynamics, and represents the integral taken over the probability space that contains the  $\boldsymbol{\omega}_m$ .

In this formulation, the connection to the Koopman operator appears in (19). The Koopman operator was originally defined for Hamiltonian systems<sup>26,27</sup>, but in recent years has also been applied to dissipative systems<sup>28,34,35,38</sup> and those with stochastic dynamics<sup>28,35</sup>; this latter formulation is most relevant here. In this application, the Koopman operator, which we denote as  $\mathcal{K}$ , is defined for a discrete-time *Markov process* with the evolution operator  $\mathbf{F}$ . The appeal of studying the Koopman operator instead of  $\mathbf{F}$ , is that  $\mathcal{K}$  is linear even when  $\mathbf{F}$  is nonlinear. However, the Koopman operator acts on scalar observables, such as the  $\psi_k$  or  $\tilde{\psi}_k$ , which map state space to scalars, and is infinite dimensional even when  $\mathbf{F}$  is finite dimensional.

For the observable  $\tilde{\psi} : \Omega_Y \rightarrow \mathbb{R}$ , the action of the Koopman operator is

$$\mathcal{K}\tilde{\psi} = \mathbb{E}[\tilde{\psi} \circ \mathbf{F}], \quad (20)$$

where  $\mathbb{E}$  is the expectation over the stochastic dynamics in  $\mathbf{F}$ , and  $\mathcal{K}\tilde{\psi} : \Omega_X \rightarrow \mathbb{R}$  is another function *defined on a*

*different domain.* With the Koopman operator, the  $ij$ -th element of  $\mathbf{A}$  can be written succinctly as

$$\mathbf{A}^{(ij)} = \langle \psi_i, \mathcal{K}\tilde{\psi}_j \rangle_\rho, \quad (21)$$

and due to the linearity of the Koopman operator, the objective function can be written as

$$g(f_X, f_Y) = \langle f_X, \mathcal{K}f_Y \rangle_\rho, \quad (22)$$

which leads to the “true” optimization problem:

$$\max_{f_X, f_Y} \langle f_X, \mathcal{K}f_Y \rangle_\rho \quad (23a)$$

$$\text{subject to: } \langle 1, f_X \rangle_\rho = \varepsilon_X, \quad (23b)$$

$$\langle 1, f_Y \rangle_\nu = \varepsilon_Y, \quad (23c)$$

$$\langle f_X, f_X \rangle_\rho = \langle f_Y, f_Y \rangle_\nu = 1, \quad (23d)$$

that we would solve if we were given an infinite amount of data and a complete set of basis functions.

As a result, one could either formulate the finite-dimensional optimization problem from the “bottom up,” as we did in Sec. II, and interpret the objective function as maximizing the number of drifters that are consistently classified at times  $n$  and  $n + 1$ , or from the “top down” as an approximation of (23). The benefit of this top down approach is that it makes the similarities between our method and the one presented in Ref. 20 clear. Because the Koopman operator,  $\mathcal{K}$ , is the adjoint of the (modified) Perron-Frobenius operator,  $\mathcal{L}$ , used there, the objective function can either be written as  $\langle f_X, \mathcal{K}f_Y \rangle_\rho$  or  $\langle \mathcal{L}f_X, f_Y \rangle_\nu$ , where the latter expression is equivalent to the objective function used by Froyland<sup>20</sup>, provided the “noise” terms are chosen appropriately. Therefore, in the limit of infinite data and a complete basis set, our approach is conceptually equivalent to the transfer operator-based methods<sup>20</sup>.

Furthermore, the problem in (10) can also be derived by approximating the Koopman operator using Extended Dynamic Mode Decomposition<sup>35</sup> with the set of snapshot pairs  $\{(\mathbf{x}_m, \mathbf{y}_m)\}_{m=1}^M$ , the basis functions  $\psi_k$  and  $\tilde{\psi}_k$ , and using Monte-Carlo integration to approximate any needed inner products. In principle, however, any method that can approximate the action of the Koopman operator directly from data, such as Generalized Laplace Analysis<sup>29</sup>, could also be “re-tasked” in order to compute coherent sets, and would lead to a different but potentially useful optimization problem.

As a result, the method outlined in Sec. II can be thought of as solving a particular approximation of (23), which the transfer operator methods also approximate using a different approach. However, the contribution of this manuscript is that our approximation allows any reasonable set of basis functions to be used, not just compactly supported ones. Because the functions of interest,  $f_X$  and  $f_Y$ , often appear to be smooth, sets of globally supported basis functions have the potential to converge much more rapidly to the solution than compactly supported ones. As we will demonstrate in the next section, this difference manifests itself in practical problems

by allowing effective (albeit not fully converged) approximations of  $f_X$  and  $f_Y$  to be obtained with fewer basis functions and therefore fewer data points than would otherwise be required.

#### IV. EXAMPLE APPLICATIONS

In this section, we consider three examples that demonstrate the efficacy of our method. The first is the double gyre, which is defined on a fixed domain, and frequently used as a “test problem” for coherent set identification. The purpose of this example is to demonstrate that the approach described here produces coherent sets that are similar to the sets produced by GAIO using an approximation of the Perron-Frobenius operator. Next, we consider the Bickley Jet, which is an idealized but more realistic problem where the data are not initially confined to some trapping region, and therefore, mesh-free approximations of  $f_X$  and  $f_Y$  becomes necessary. Next, we consider the example of numerically simulated “drifters” in the Sulu Sea, which is a realistic example of how we envision this technique being used in practice. In this example, our objective is to identify an eddy that is already known to exist in the time frame of the simulation.

##### A. Choosing the Basis Functions

As mentioned previously, one important facet of this procedure is the choice of the basis functions that are the building blocks for  $\psi_X$  and  $\psi_Y$ . In each of these problems, we use a basis set of thin-plate splines, which are functions of the form:

$$\psi_k(\mathbf{x}) = r^2 \log(r), \quad \text{where } r = \|\mathbf{x} - \boldsymbol{\xi}_k\|, \quad (24a)$$

$$\tilde{\psi}_k(\mathbf{y}) = \tilde{r}^2 \log(\tilde{r}), \quad \text{where } \tilde{r} = \|\mathbf{y} - \tilde{\boldsymbol{\xi}}_k\|, \quad (24b)$$

where  $\boldsymbol{\xi}_k$  is the  $k$ -th radial basis function (RBF) center, which is a vector in  $\mathbb{R}^N$  that defines the “location” of the thin plate spline. We also define the basis functions used to construct  $f_Y$  in a similar manner, but call the associated centers  $\tilde{\boldsymbol{\xi}}_k$ . This type of basis set was chosen primarily because it does not require a computational mesh to be defined (i.e., it is a so-called “mesh-free” method)<sup>39–41</sup>. The  $\boldsymbol{\xi}_k$  and  $\tilde{\boldsymbol{\xi}}_k$  are chosen by applying  $k$ -means clustering<sup>42</sup> to the collection of  $\mathbf{x}_m$  and  $\mathbf{y}_m$  snapshots respectively.  $k$ -means clustering partitions a set of data into  $k$ -sets, which are chosen to minimize the total distance between the points and the mean of the set they are assigned to. We use the set of means that result from this procedure as the  $\boldsymbol{\xi}_k$  and  $\tilde{\boldsymbol{\xi}}_k$  respectively.

To determine the number of basis functions,  $K_X$  and  $K_Y$ , we first choose a “conservative” pair of values, say,  $K = K_X = K_Y = 5$ . Next we compute the leading singular value of the  $\hat{\mathbf{A}}$  associated with the basis sets generated by this value of  $K$ . If the leading singular value is one, then we increment  $K$ , and repeat the process until

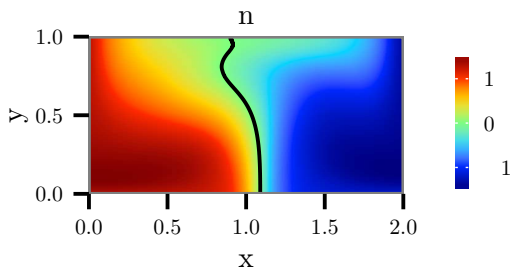


Figure 2. The function equivalent to  $f_X$  computed using GAIO with 262,144 indicator functions (and the equivalent of 104,857,600 data pairs). The black line denotes the zero level set of both functions, which would be used to partition the domain into two coherent sets.

this constraint fails to hold. The results in this section are from the largest value of  $k$  that did not violate our “sanity check,” which as a “rule of thumb,” corresponds to between 5-20 data points per basis function. This procedure is *ad hoc*, but appears to produce a useful and “rich” set of basis functions for the examples presented in this manuscript.

This is, of course, not the only possible choice of basis functions, nor do we claim it is in any way optimal. Indeed, other basis sets may have superior performance for either or even both of our examples. However, the benefit of using mesh-free basis elements like the thin plate splines is that they can be applied to problems on domains that are not simple rectangles, which makes them suitable for a wide range of applications. This allows us to apply the same procedure, without any changes, to both of the examples that follow despite the fact that one is defined on a fixed domain and the other is not.

## B. The Double Gyre

Our first example is the double gyre, whose governing equations are:

$$\dot{x} = -\pi A \sin(\pi h(x, t)) \cos(\pi y), \quad (25a)$$

$$\dot{y} = \pi A \cos(\pi h(x, t)) \sin(\pi y), \quad (25b)$$

where  $h(x, t) = \epsilon \sin(\omega t)x^2 + (1 - 2\epsilon \sin(\omega t))x$  with  $\epsilon = 0.25$ ,  $\omega = 2\pi$ , and  $A = 0.25$ . In these equations,  $x \in [0, 2]$  and  $y \in [0, 1]$ . The double gyre with these parameters is a frequently used “test case” for coherent structure computations. See, for example, Refs. 6,21,30, which compute coherent sets (albeit with slightly different definitions) for this problem and parameters.

The purpose of this example is to demonstrate that the computational procedure outlined in Sec. II produces coherent sets that are similar to those produced using the definition in Refs. 17,18,20,21, from a more limited amount of data. For the purposes of comparison, Fig. 2 shows the equivalent of  $f_X$  identified by GAIO, which uses 262,144 indicator functions and a total of

104,857,600 data pairs (i.e., 400 points per function). Because it uses indicator functions, a large basis set and, hence, a large amount of data is required if the resulting functions are to “look smooth.” By using tree-like data structures, this computation can be performed quickly even with hundreds of millions of data points<sup>23</sup>. However, in applications where experimental rather than numerical data is being used, obtaining such a large set may not be possible.

To highlight the performance of the method, we apply it with 51, 251, and 501 basis functions (e.g., 50 thin plate splines and the constant function) using 1000, 5000, and 10,000 data pairs respectively. The data at the initial time (i.e., the  $\mathbf{x}_m$ ) are chosen by randomly selecting initial conditions from a uniform distribution on state space. Because the governing equations are discrete, we make the system stochastic by adding noise to the  $\mathbf{y}_m$ . In this example, we make 20 “copies” of each of our data pairs and perturb the data by adding a random vector chosen from normal distribution with a standard deviation of  $10^{-3}$ ; with the basis sets we will use, neither the number of copies nor the precise nature of the noise will have a qualitative impact on the resulting functions. As a result, the values of  $M$  in our computation are 20,000, 100,000, and 200,000, which accounts for these additional copies, but similar results could be obtained in the “noiseless” case with  $M = 1000$ , 5000, and 10,000. Finally, we impose that  $\varepsilon_X = \varepsilon_Y = 0$  in order to facilitate comparison with GAIO.

Figure 3 shows the function,  $f_X$ , obtained using the three sets of data listed above. The black line denotes the  $f_X = 0$  level set, which is used to partition state space into the pair of coherent sets. As shown above, our approximations of  $f_X$  appear to be converging to a particular function as the number of basis functions and data points increases; when run with 1,001 basis functions and 20,000 sets of data ( $M = 4 \times 10^5$ ) the resulting  $f_X$  is qualitatively similar to the function obtained with 501 basis functions.

As a benchmark for our approach, Fig. 4 shows the function equivalent to  $f_X$  computed using GAIO with 64, 256, and 512 basis functions with 25 data points per basis function initialized on a uniform grid. This figure should be compared to Fig. 3, which used slightly fewer basis functions (i.e., 51, 251, and 501) with 20 randomly distributed initial conditions per basis function. As a result, each column in Fig. 3 and Fig. 4 are comparable. The most apparent difference between these two sets of results is the smoothness of  $f_X$ , which are both clearly discontinuous in Fig. 4 due to the basis set that is implicitly chosen by GAIO. More importantly for experimental applications, we obtain a solution that is *qualitatively* similar to the “true” solution with only 251 basis functions, while GAIO requires at least twice that amount of data.

We should note that there are quantitative differences between the coherent sets identified using our method and the ones identified by GAIO. In particular, there are



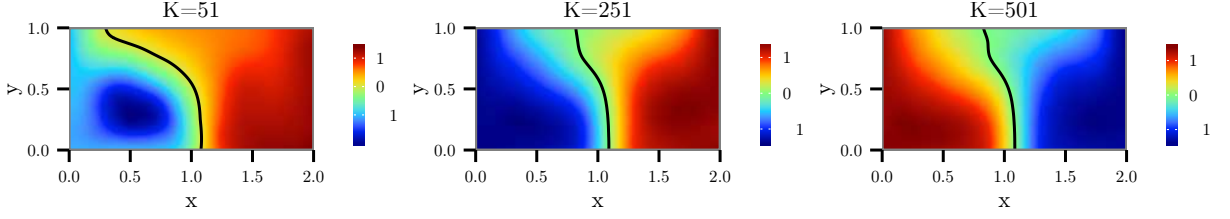


Figure 3. The function  $f_X$  for the double gyre computed using 51, 251, and 501 basis functions (e.g., 50 thin plate splines and the constant function) with  $\varepsilon_X = \varepsilon_Y = 0$ . The black line indicates the zero level set, which partitions the domain into the two sets  $X_1$  and  $X_2$ . These results should be compared with the “true” solution in Fig. 2.

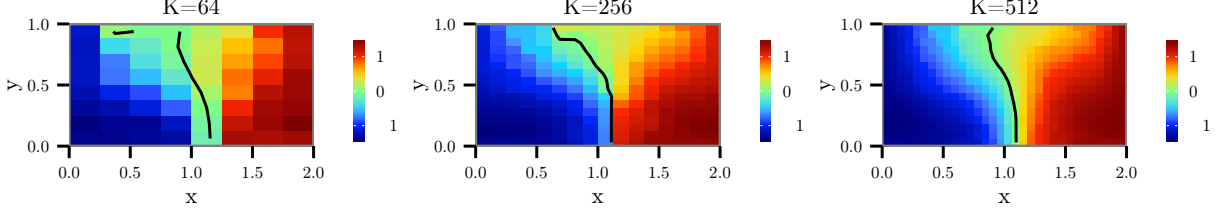


Figure 4. The function equivalent to  $f_X$  obtained using GAIO with 64, 256, and 512 basis functions and 25 uniformly distributed data points per basis function; the images here are a benchmark for our results, which are shown in Fig. 3.

small quantitative differences in the zero level sets near the point  $x = 1$  and  $y = 1$  for  $f_X$  and  $x = 1$  and  $y = 0$  for  $f_Y$ . Part of this difference is due to the “noise” added to the data; our approach explicitly adds normally distributed perturbations, and GAIO *implicitly* adds noise that is related to the width of each subdomain<sup>20</sup>. As a result, the part of the error due to differences in the added noise would not vanish even if the amount of data was effectively infinite. However, there is also a difference in the spaces spanned by the thin plate splines used here and the indicator functions used by GAIO. In particular, a large number of thin plate splines would be required to capture the sudden “bulge” that occurs in  $f_X$  near the edge of the domain. However, more data is still useful if highly accurate approximations are desired, as the part of the error due to a lack of basis functions could be reduced.

As shown here, our approach compares favorably to the Perron-Frobenius based methods for coherent set identification, and produces coherent pairs that are qualitatively similar to the ones identified by those methods. Given access to a black-box simulator, either method is viable and choosing between our approach and GAIO is the same choice as deciding between a spectral method<sup>31,32</sup> and a finite-volume method<sup>33</sup>. Like a spectral method, our approach uses fewer basis functions that are globally supported, but appears to converge rapidly provided  $f_X$  and  $f_Y$  are smooth. On the other hand, GAIO needs larger sets of basis functions, but produces matrices that are sparse; as a result, using a large number of basis functions and large quantities of data is computationally tractable.

### C. The Bickley Jet

In this example, we demonstrate the effectiveness of this method by computing a pair of coherent sets in the Bickley Jet flow which is a dynamically-consistent approximation of an idealized stratospheric flow<sup>43</sup>. We are concerned with sets that are optimal for the interval  $t \in [10, 20]$  days, which was chosen so that these results may be compared with pre-existing results<sup>21</sup>. By making use of “mesh-free” basis functions, such as the thin plate splines, the same procedure used on the double gyre can also be applied here without modification.

This idealized system is Hamiltonian:

$$\frac{\partial x}{\partial t} = -\frac{\partial \Phi}{\partial y}, \quad (26a)$$

$$\frac{\partial y}{\partial t} = \frac{\partial \Phi}{\partial x}, \quad (26b)$$

where

$$\begin{aligned} \Phi(x, y, t) = & c_3 y + U_0 L \tanh(y/L) \\ & + A_3 U_0 L \operatorname{sech}^2(y/L) \cos(k_3 x) \\ & + A_2 U_0 L \operatorname{sech}^2(y/L) \cos(k_2 x - \sigma_2 t) \\ & + A_1 U_0 L \operatorname{sech}^2(y/L) \cos(k_1 x - \sigma_1 t), \end{aligned} \quad (26c)$$

with  $U_0 = 5.41$ ,  $L = 1.770$ ,  $c_2 = 0.205U_0$ ,  $c_3 = 0.7U_0$ ,  $A_1 = 0.075$ ,  $A_2 = 0.4$ ,  $A_3 = 0.2$ ,  $k_1 = 2/r_c$ ,  $k_2 = 4/r_c$ ,  $k_3 = 6/r_c$ ,  $r_c = 6.371$ ,  $\sigma_2 = k_2(c_2 - c_3)$ , and  $\sigma_1 = \frac{1+\sqrt{5}}{2}\sigma_2$ . See Rypina *et al.*<sup>43</sup> for an explanation of these parameter values. Our initial data are  $10^4$  uniformly distributed on  $x \in [0, 20]$  and  $y \in [-2.5, 2.5]$  at  $t = 10$  days, but many initial points will leave this window in this interval. As with the double gyre, we augment our data set

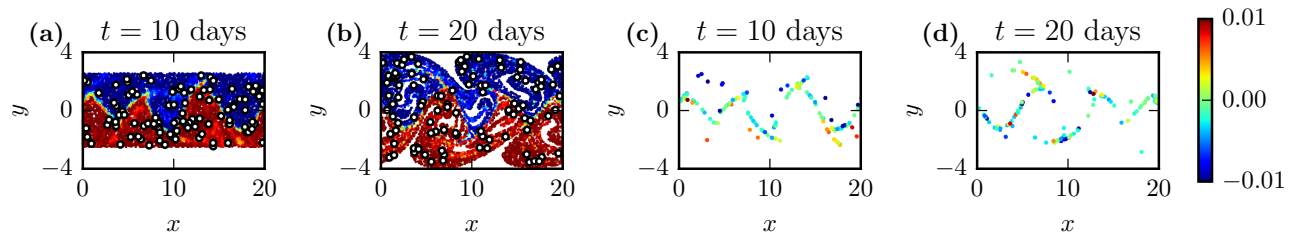


Figure 5. (a) The  $10^4$  data points that comprise the data set colored by the numerically computed approximation of  $f_X$ . (b) The set of points in (a) at their new positions at  $t = 20$  days; note that these points are still colored by  $f_X$  rather than  $f_Y$ . (c) The set of 129 mis-classified points (i.e., those that “leaked” out over the 10 day window) at  $t = 10$  days. (d) The same set of points at  $t = 20$  days. The white circles in the left two images represent 100 of the 1000  $\xi_k$  and  $\tilde{\xi}_k$  that were used as the centers of the radial basis functions. Despite the complexity of the “true” coherent sets and the relatively small number of basis functions, there is little mixing between the numerically computed sets, and most of the mixing occurs on the boundary between the sets or in thin filaments extending into either side.

with 20 “copies” of the data, where  $\mathbf{y}_m$  the perturbed randomly using numbers drawn from a normal distribution with a standard deviation of  $10^{-3}$ . Because our initial box is not a trapping region of the dynamical system in the  $y$ -direction, choosing different basis functions to represent  $f_X$  and  $f_Y$  is critical because  $\Omega_X \neq \Omega_Y$ . Here, we use  $10^3$  thin plate splines whose centers are chosen using the  $k$ -means procedure outlined at the start of this section. Unlike the double gyre, where the basis functions used to approximate  $f_X$  and  $f_Y$  were effectively identical, because the distribution of the data points at  $t = 10$  and  $t = 20$  days is different, the difference in the  $\psi_k$  and  $\tilde{\psi}_k$  now become important. Visually, the differences in the centers are indicated by the white dots in Fig. 5, which indicate the position of a subset of the centers of the thin plate splines.

Figure 5 shows the results obtained with these basis functions and data. Unlike the double gyre where  $f_X$  and  $f_Y$  were relatively simple, the geometry of the coherent pair is more complex for the Bickley Jet, and both sets have a “sawtooth” pattern. Like the double gyre, the function in Fig. 5a changes rapidly in value from approximately -0.015 to 0.015 at the boundary between the coherent pair. To highlight the rate at which the function values change, the color-scale in those figures is restricted to -0.01 to 0.01 rather than the full range of values. The sets identified by partitioning the data based on the sign of  $f_X$  with  $10^4$  data points compares favorably with those Ref. 21, which uses over a million data points. In particular, we partition the computational domain into the two subdomains that are located above and below the oscillating jet near  $y = 0$  that separates them. Furthermore, as shown in the figure, this approximation is “good enough” that only 129 of the  $10^4$  numerically classified points “leak” out of the set they were assigned to; similar to Refs. 19,21, this leakage occurs either on the boundary between sets or on thin filaments that penetrate into either side.

This example highlights the fact that with the right choice of basis functions, such as the globally supported

thin plate splines, the same procedure (without any modification) can be applied to problems with non-trivial coherent sets on domains that vary with time. In such applications, using different basis functions to represent  $f_X$  and  $f_Y$  is critical, and in this example, this difference manifests itself in the centers chosen for the thin plate splines, which differ at times  $n$  and  $n + 1$ . It should be noted, however, that the numerical procedure for generating these basis functions is the same one used in the double gyre example: the  $k$ -means clustering process automatically accounts for the differences in the  $\mathbf{x}_m$  and  $\mathbf{y}_m$  data.

#### D. Numerical Drifters in the Sulu Sea

In this section, we consider a more realistic example generated by a numerical model ROMS<sup>44</sup> for the Philippine Archipelago<sup>10</sup>. Similar to the work of Rypina *et al.*<sup>10</sup>, the objective here is to use our coherent set definition to identify a mesoscale anticyclonic eddy that was present in the Sulu Sea. Our data come in the form of numerically simulated drifters, that are sampled once every week. These drifters are randomly and uniformly distributed over the computational domain. In an experiment rather than a simulation, initializing thousands of drifters is infeasible, and so the data available are truly limited in quantity. As such, we consider two cases: the first consists of 25,146 tracers randomly but uniformly distributed over the computational domain, and constitutes a “data rich” example, which we will use to determine the “true” coherent sets. Then we will reduce the amount of data to 400 uniformly but randomly distributed initial conditions, which is a more realistic amount of data, and compare the results obtained from this “data poor” set with the full data. As before, we make 20 copies of the data and add normally distributed noise with a standard deviation of 5 km to the elements of the  $\mathbf{y}_m$ .

In this example, we are interested in identifying a

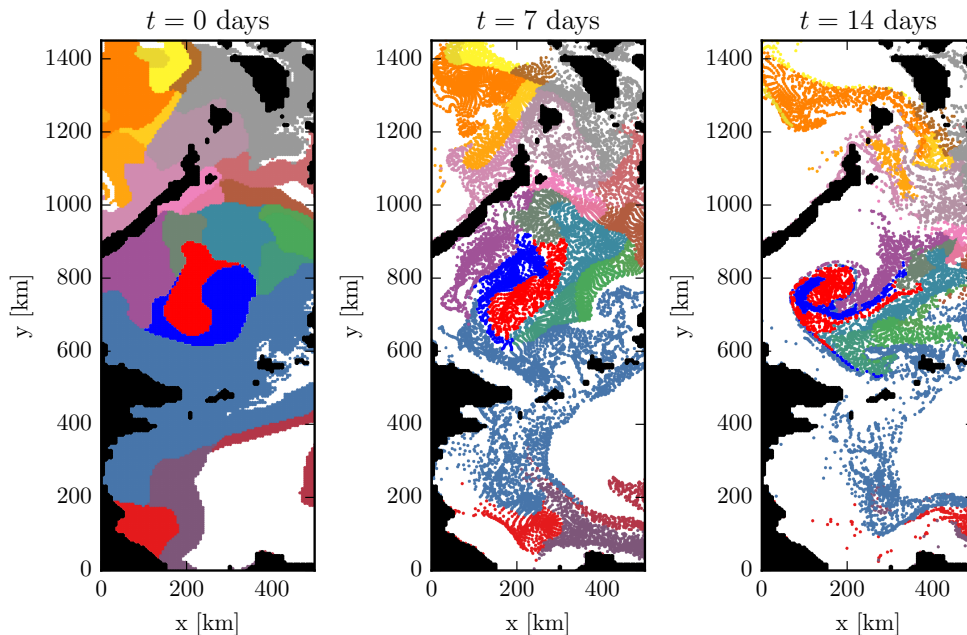


Figure 6. The three images above show the evolution of the “complete” set of 25,146 data points at  $t = 0$ , 7, and 14 days. Two of the 27 coherent sets identified by the method, which correspond to the eddy of interest, are shown in red and blue; the other 25 sets are indicated by the other colors. In all three images, the black points denote land. It should be noted that these coherent sets are only optimal from  $t = 0$  to 7 days. At  $t = 14$  days, this lack of optimality can be seen in the long filaments that have formed in the blue and red sets.

mesoscale eddy with a 100-km radius within a much larger, 500 km by 1500 km, domain. While both the “rich” and “poor” data sets can be partitioned into a pair of coherent sets, due to the implicit constraint on the size of these sets, neither will immediately identify the eddy of interest. Therefore, it becomes necessary to iterate the procedure and to further subdivide space until the size of the coherent sets is on the same order as the eddy. As a result, we will iterate up to four times using the procedure described in Sec. II and Refs. 21,30. For each of the iterates, we choose  $\varepsilon_X$  and  $\varepsilon_Y$  to maximize the fraction of consistently classified data pairs. We limit the range of values that the  $\varepsilon_X$  and  $\varepsilon_Y$  can take on so that the resulting sets contain (roughly) the same number of points (i.e., the smaller set must contain at least 25% of the total data). This additional restriction is *ad hoc*, and meant to prevent the algorithm from selecting “trivial” sets with only a handful of isolated data points. Initially we use 250 basis functions for the full data, and 40 for the reduced data set of 400 points. After every subsequent iteration, we divide the number of basis functions used in the computation by two and require that the number of basis functions is no more than 10% of the data points; as a result, later iterations are performed on smaller domains and with fewer basis functions.

In Fig. 6, we show the hierarchy of coherent sets that is optimal for the  $t = 0$  to  $t = 7$  days time window using the full set of the 25,146 data points available, where each of the points are “colored” by the set they were assigned

to. There is an additional plot of the data at  $t = 14$  days that demonstrates that the coherent sets identified by our method remain coherent even at longer times. We should reiterate, however, that these sets are, by construction, only optimal from  $t = 0$  to 7 days; the results at  $t = 14$  days are extrapolation, and not guaranteed to still be coherent at that time. In this example, the persistence of the identified coherent sets until day 14 is consistent with Rypina *et al.*<sup>10</sup> who also found the eddy to be present over a 2-week period. Note that even at  $t = 0$  the data has “holes,” which are due either to the presence of land, which is indicated by the black regions, or because initial conditions at those regions leave the computational window in Fig. 6 before a week has elapsed.

The identified coherent sets are “optimal” sets, but that does not necessarily mean that all of them necessarily have a simple and straightforward physical interpretation. However, one physically meaningful pair of coherent sets is indicated by the red and blue regions near  $x = 200$  km and  $y = 700$  km in the figure, and corresponds to the eddy identified by Rypina *et al.*<sup>10</sup>. From  $t = 0$  to  $t = 7$ , the red and blue sets move counterclockwise around each other without much stretching and folding, which would be typical for a cyclonic motion associated with an eddy. Note however, that because the sets are not optimal at  $t = 14$  days, they begin to leak out of the eddy at that time forming long filaments. To summarize, with a large amount of drifter data, such as the dataset generated numerically using the velocity field,

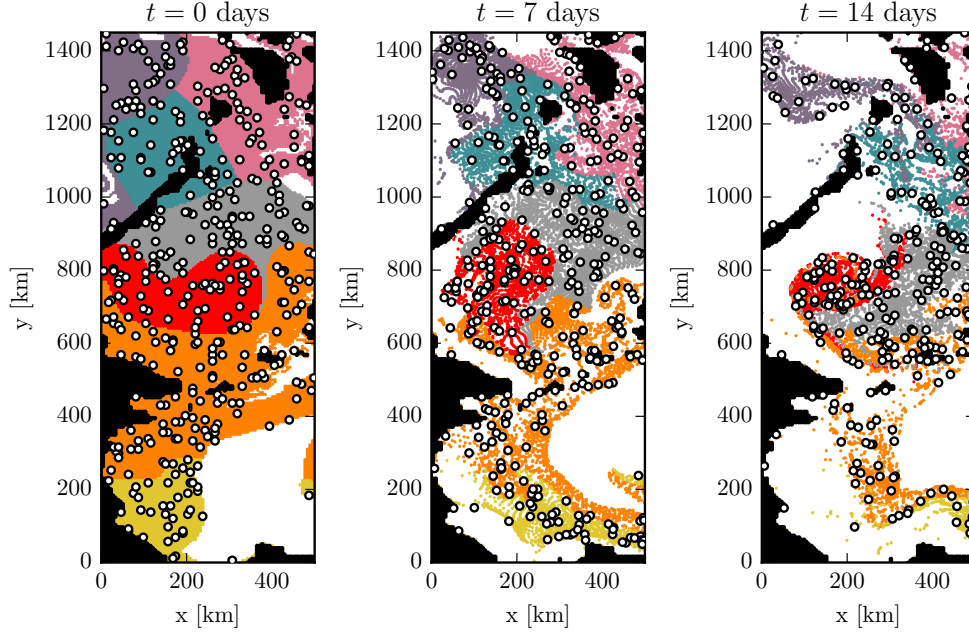


Figure 7. This is a reproduction of Fig. 6 using only the 400 data points indicated by the white dots. As in that figure, the other 24,746 points are colored based on which coherent set they are assigned to by the approximation of  $f_X$  obtained from the indicated set of 400 points. Note that the eddy is once again identified, but is now contained within a single coherent set that is shown in red.

this approach can produce a partition of state space that contains physically meaningful time-varying sets.

However, the purpose of this manuscript is to demonstrate that these results can be obtained with limited quantities of Lagrangian data, so we repeat the computation above with 400 data points instead of the full set of 25,146. We follow the same iteration procedure as before, and compute additional sets by recursing up to four times provided the identified coherent sets “mis-classified” at most 5% of the data points in the computation. The results of this computation are shown in Fig. 7. To aid the eye, the colored points are, once again, the complete data set that is shown in Fig. 6, where the colors denote the various coherent sets. The 400 points used in the computation are indicated by the large white dots in the figure.

As shown, the relatively small amount of data and the concomitant reduction in the number of basis functions has had an impact on the resolution and accuracy of the resulting method. Visually, the coherent sets we identify are larger in area than those that we obtain with full data because fewer iterations of the coherent set algorithm can be performed before our sets allow more than 5% of their points to escape. Nonetheless, we once again identify the eddy, which is now indicated solely by the red set. Once again, this set is only optimal from  $t = 0$  to 7 days, and long filaments are again visible at  $t = 14$  days.

It should be noted that whether the eddy is contained within a single coherent set or a pair of coherent sets is de-

termined by the basis functions and data provided to the method. The “data rich” example subdivides the eddy after the 2nd iteration of the procedure, when the coherent sets are still much larger than the red region shown in Fig. 7. As a result, the results in the “data poor” example are not equivalent to the results we would obtain if we terminated the iterative procedure used in the data rich case sooner. Our algorithm can capture the eddy with a single coherent set if the standard deviation of the added noise is increased to 20 km. However, because the size of eddy is on the order of 100 km, at this point the noise is no longer relatively small on the length scales of interest, and the precise distribution of the added noise can no longer be neglected.

In this section, we applied our algorithm to compute coherent sets in a more realistic problem, and identified a eddy that is known to exist in this flow. Because this coherent set algorithm has not previously been applied to this data set, we first computed the coherent sets using the entirety of the data to show that this approach can, under ideal conditions, pick out physically meaningful coherent structures. Then we limited the amount of data we had access to, and repeated the computation. Intuitively, more data is “better,” and the results of this section reflect that; however, even with a very limited amount of data, our approach was able to identify useful and physically meaningful coherent sets in the data.

## V. CONCLUSIONS

In this manuscript, we presented a method for computing coherent sets that are optimal over a finite interval in time, which in the limit of infinite data is (effectively) equivalent to the definition presented by Froyland<sup>20</sup>. While the two approaches are conceptually related, in practice, the implementations are different due to the way the functions that define the coherent sets,  $f_X$  and  $f_Y$ , are approximated, and how “noise” is injected in order to make a deterministic system stochastic. Assuming the noise is chosen appropriately, both methods effectively converge to the same pair of coherent sets given an infinitely large amount of data and a “rich enough” set of basis functions.

However, our interest here is in the “data poor” regime, which is common in problems involving experimental, rather than computational, experiments where the velocity field is unknown and exhaustive sampling infeasible. In the double gyre example, we demonstrated that the coherent sets identified using a limited number of thin plate splines agreed well with the sets obtained using a larger number of indicator functions. Because this particular example is defined on a rectangular domain, other basis sets such as, say, Legendre polynomials would yield superior performance. The benefit of using thin plate splines or other mesh-free basis functions is that they can also be used in problems where a computational grid is not easily defined. This is useful in the second example involving the Bickley Jet, where the initial domain is not a trapping region, and the domain at the final time resembles a “sawtooth.” By using radial basis functions, the same procedure used for the double gyre can also be used here without alteration. Our final example is identifying an eddy in the Sulu Sea, which possessed a changing computational domain in combination with a relatively small coherent set of physical interest. In that example, we also demonstrated that our approach can identify the eddy of interest even with relatively small amounts of data that approach the number of drifters used in recent massive drifter deployment experiments<sup>45,46</sup>.

In all three examples, the noise added to the system was normally distributed with a standard deviation that was small compared to the spatial scales on which the problem was defined. With the data available to us, any reasonable choice of noise appears to produce qualitatively similar results, but the existence of stochasticity is conceptually important if defined coherent sets are to exist in the infinite data limit. One improvement to the procedure would be to use observation-based spatially-dependent anisotropic diffusivities (see, for example, Rypina *et al.*<sup>47</sup>) to represent the stochastic portion of the flow instead of arbitrarily choosing a distribution. When the amplitude of the added noise is small, the precise distribution of the “noise” appears to have little impact on the qualitative shape of the resulting sets. However, when the noise is “large”, then the distribution can matter; therefore, a physically motivated rather than

*ad hoc* stochastic term will become necessary.

Because of the crucial role transport barriers play in understanding systems with chaotic mixing, algorithmic methods for identifying these barriers are useful tools for researchers in application areas like geophysical fluid dynamics, combustion, and even those focused on ecological problems. In some situations, one either knows or can approximate the velocity field of the flow, which enables standard techniques and software packages such as FTLE fields or GAIO to be used. However, in other applications, the velocity field cannot be obtained analytically or numerically, and Lagrangian data from drifting buoys are all that is available to us. Ultimately, algorithms such as the one presented here are the first steps towards adapting the techniques we would use in a data rich environment for use in practical problems where the needed Lagrangian data are sparse and difficult/expensive to obtain.

## ACKNOWLEDGMENTS

The authors would like to acknowledge I.G. Kevrekidis for helpful discussions on set-oriented methods and suggestions for this manuscript. M.O.W. gratefully acknowledges support from the NSF (DMS-1204783). I.R. was supported by ONR (MURI award N000141110087), and by the NSF (grant 85464100). C.W.R. was supported by AFOSR (grant FA9550-14-1-0289).

## Appendix A: The Leading Singular Vectors of the Approximation

To prove that the first unit vectors are also singular vectors of  $\hat{\mathbf{A}}$ , we must first prove that  $\hat{\mathbf{A}}$  is block diagonal. To show this structure arises, it is convenient to define the data matrices

$$\Psi_X = \begin{bmatrix} \psi_X(\mathbf{x}_1)^T \\ \psi_X(\mathbf{x}_2)^T \\ \vdots \\ \psi_X(\mathbf{x}_M)^T \end{bmatrix}, \quad \Psi_Y = \begin{bmatrix} \psi_Y(\mathbf{y}_1)^T \\ \psi_Y(\mathbf{y}_2)^T \\ \vdots \\ \psi_Y(\mathbf{y}_M)^T \end{bmatrix}, \quad (\text{A1})$$

where  $\Psi_X \in \mathbb{R}^{M \times K_X}$  and  $\Psi_Y \in \mathbb{R}^{M \times K_Y}$ . Note that  $\mathbf{A} = \frac{1}{M} \Psi_X^T \Psi_Y$ ,  $\mathbf{G}_X = \frac{1}{M} \Psi_X^T \Psi_X$ , and  $\mathbf{G}_Y = \frac{1}{M} \Psi_Y^T \Psi_Y$ .

Because the Cholesky Decomposition is unique, we can also write

$$\Psi_X = \sqrt{M} \mathbf{Q}_X \mathbf{L}_X^T, \quad \text{and} \quad \Psi_Y = \sqrt{M} \mathbf{Q}_Y \mathbf{L}_Y^T, \quad (\text{A2})$$

where  $\mathbf{Q}_X$  and  $\mathbf{Q}_Y$  are orthonormal matrices. While  $\mathbf{Q}_X$  and  $\mathbf{Q}_Y$ , in general, differ, this is a QR decomposition, so the first columns of  $\mathbf{Q}_X$  and  $\mathbf{Q}_Y$  are normalized version of the first columns of  $\Psi_X$  and  $\Psi_Y$ . However, because of our choice of basis functions (in particular,  $\psi_1 = \tilde{\psi}_1 = 1$ ), the first columns of  $\Psi_X$  and  $\Psi_Y$  are identical. Therefore, the first columns of  $\mathbf{Q}_X$  and  $\mathbf{Q}_Y$ , which we refer to as  $\mathbf{q}_X^{(1)}$



and  $\mathbf{q}_Y^{(1)}$ , are also identical. Furthermore,  $\mathbf{Q}_Y^T \mathbf{q}_X^{(1)} = \tilde{\mathbf{e}}_1$  and  $\mathbf{Q}_X^T \mathbf{q}_Y^{(1)} = \mathbf{e}_1$  by the orthonormality of  $\mathbf{Q}_X$  and  $\mathbf{Q}_Y$ . Finally,  $\hat{\mathbf{A}} = \mathbf{L}_X^{-1} \mathbf{A} \mathbf{L}_Y^{-T} = \mathbf{L}_X^{-1} \mathbf{L}_X (\mathbf{Q}_X^T \mathbf{Q}_Y) \mathbf{L}_Y^T \mathbf{L}_Y^{-T} = \mathbf{Q}_X^T \mathbf{Q}_Y$ . Because the first columns of  $\mathbf{Q}_X$  and  $\mathbf{Q}_Y$  are identical

$$\hat{\mathbf{A}} = \mathbf{Q}_X^T \mathbf{Q}_Y = \begin{bmatrix} 1 & \mathbf{0} \\ \mathbf{0} & \hat{\mathbf{A}}_{22} \end{bmatrix}, \quad (\text{A3})$$

which shows the matrix  $\hat{\mathbf{A}}$  possess the desired block structure. Because of this structure, it is now clear that  $\mathbf{e}_1$  and  $\tilde{\mathbf{e}}_1$  are singular vectors associated with the singular value  $\sigma = 1$ .

By enforcing that  $\psi_1 = \tilde{\psi}_1 = 1$ , we guarantee that  $\hat{\mathbf{A}}$  has this form, but this is a sufficient rather than necessary condition. Certain basis sets, such as indicator functions (see, e.g., Refs. 17,18,21), will also have a singular value of 1 without being “rearranged.” However, because rearranging the basis functions does not deleteriously impact the algorithm, we will assume this has been done regardless of whether or not it is necessary.

## REFERENCES

- <sup>1</sup>J. Ottino, “Mixing, chaotic advection, and turbulence,” *Annual Review of Fluid Mechanics* **22**, 207–254 (1990).
- <sup>2</sup>H. Aref, “The development of chaotic advection,” *Physics of Fluids* **14**, 1315–1325 (2002).
- <sup>3</sup>S. Wiggins, “The dynamical systems approach to Lagrangian transport in oceanic flows,” *Annu. Rev. Fluid Mech.* **37**, 295–328 (2005).
- <sup>4</sup>I. Mezić, S. Loire, V. A. Fonoberov, and P. Hogan, “A new mixing diagnostic and Gulf oil spill movement,” *Science* **330**, 486–489 (2010).
- <sup>5</sup>M. J. Olascoaga and G. Haller, “Forecasting sudden changes in environmental pollution patterns,” *Proceedings of the National Academy of Sciences* **109**, 4738–4743 (2012).
- <sup>6</sup>T. Ma and E. Bollt, “Shape coherence and finite-time curvature evolution,” *arXiv preprint arXiv:1405.1758* (2014).
- <sup>7</sup>G. Haller, “Finding finite-time invariant manifolds in two-dimensional velocity fields,” *Chaos: An Interdisciplinary Journal of Nonlinear Science* **10**, 99–108 (2000).
- <sup>8</sup>S. L. Brunton and C. W. Rowley, “Fast computation of finite-time Lyapunov exponent fields for unsteady flows,” *Chaos: An Interdisciplinary Journal of Nonlinear Science* **20**, 017503 (2010).
- <sup>9</sup>S. C. Shadden, F. Lekien, and J. E. Marsden, “Definition and properties of Lagrangian coherent structures from finite-time Lyapunov exponents in two-dimensional aperiodic flows,” *Physica D: Nonlinear Phenomena* **212**, 271–304 (2005).
- <sup>10</sup>I. I. Rypina, L. J. Pratt, J. Pullen, J. Levin, and A. L. Gordon, “Chaotic advection in an archipelago\*,” *Journal of Physical Oceanography* **40**, 1988–2006 (2010).
- <sup>11</sup>G. Haller and G. Yuan, “Lagrangian coherent structures and mixing in two-dimensional turbulence,” *Physica D: Nonlinear Phenomena* **147**, 352–370 (2000).
- <sup>12</sup>I. I. Rypina, S. Scott, L. J. Pratt, and M. G. Brown, “Investigating the connection between complexity of isolated trajectories and Lagrangian coherent structures,” *Nonlinear Processes in Geophysics* **18**, 977–987 (2011).
- <sup>13</sup>G. Haller and T. Sapsis, “Lagrangian coherent structures and the smallest finite-time Lyapunov exponent,” *Chaos: An Interdisciplinary Journal of Nonlinear Science* **21**, 023115 (2011).
- <sup>14</sup>F. J. Beron-Vera, Y. Wang, M. J. Olascoaga, G. J. Goni, and G. Haller, “Objective detection of oceanic eddies and the agulhas leakage,” *Journal of Physical Oceanography* **43**, 1426–1438 (2013).
- <sup>15</sup>M. Budišić and I. Mezić, “Geometry of the ergodic quotient reveals coherent structures in flows,” *Physica D: Nonlinear Phenomena* **241**, 1255–1269 (2012).
- <sup>16</sup>C. Mendoza, A. Mancho, and S. Wiggins, “Lagrangian descriptors and the assessment of the predictive capacity of oceanic data sets,” *Nonlinear Processes in Geophysics* **21**, 677–689 (2014).
- <sup>17</sup>G. Froyland, K. Padberg, M. H. England, and A. M. Treguier, “Detection of coherent oceanic structures via transfer operators,” *Physical review letters* **98**, 224503 (2007).
- <sup>18</sup>G. Froyland, S. Lloyd, and N. Santitissadeekorn, “Coherent sets for nonautonomous dynamical systems,” *Physica D: Nonlinear Phenomena* **239**, 1527–1541 (2010).
- <sup>19</sup>G. Froyland, N. Santitissadeekorn, and A. Monahan, “Transport in time-dependent dynamical systems: Finite-time coherent sets,” *Chaos: An Interdisciplinary Journal of Nonlinear Science* **20**, 043116 (2010).
- <sup>20</sup>G. Froyland, “An analytic framework for identifying finite-time coherent sets in time-dependent dynamical systems,” *Physica D: Nonlinear Phenomena* **250**, 1–19 (2013).
- <sup>21</sup>E. M. Bollt and N. Santitissadeekorn, *Applied and Computational Measurable Dynamics*, Vol. 18 (SIAM, 2013).
- <sup>22</sup>G. Froyland and K. Padberg, “Almost-invariant sets and invariant manifolds – connecting probabilistic and geometric descriptions of coherent structures in flows,” *Physica D: Nonlinear Phenomena* **238**, 1507–1523 (2009).
- <sup>23</sup>M. Dellnitz, G. Froyland, and O. Junge, “The algorithms behind GAIO – set oriented numerical methods for dynamical systems,” in *Ergodic theory, analysis, and efficient simulation of dynamical systems* (Springer, 2001) pp. 145–174.
- <sup>24</sup>B. K. Horn and B. G. Schunck, “Determining optical flow,” in *1981 Technical Symposium East* (International Society for Optics and Photonics, 1981) pp. 319–331.
- <sup>25</sup>F. A. Mussa-Ivaldi, “From basis functions to basis fields: vector field approximation from sparse data,” *Biological cybernetics* **67**, 479–489 (1992).
- <sup>26</sup>B. O. Koopman, “Hamiltonian systems and transformation in Hilbert space,” *Proceedings of the National Academy of Sciences of the United States of America* **17**, 315 (1931).
- <sup>27</sup>B. Koopman and J. v. Neumann, “Dynamical systems of continuous spectra,” *Proceedings of the National Academy of Sciences of the United States of America* **18**, 255 (1932).
- <sup>28</sup>I. Mezić, “Spectral properties of dynamical systems, model reduction and decompositions,” *Nonlinear Dynamics* **41**, 309–325 (2005).
- <sup>29</sup>M. Budišić, R. Mohr, and I. Mezić, “Applied Koopmanism,” *Chaos: An Interdisciplinary Journal of Nonlinear Science* **22**, 047510 (2012).
- <sup>30</sup>T. Ma and E. M. Bollt, “Relatively coherent sets as a hierarchical partition method,” *International Journal of Bifurcation and Chaos* **23** (2013).
- <sup>31</sup>L. N. Trefethen, *Spectral methods in MATLAB*, Vol. 10 (Siam, 2000).
- <sup>32</sup>J. P. Boyd, *Chebyshev and Fourier spectral methods* (Courier Dover Publications, 2013).
- <sup>33</sup>R. J. LeVeque, *Finite volume methods for hyperbolic problems*, Vol. 31 (Cambridge university press, 2002).
- <sup>34</sup>I. Mezić, “Analysis of fluid flows via spectral properties of the Koopman operator,” *Annual Review of Fluid Mechanics* **45**, 357–378 (2013).
- <sup>35</sup>M. O. Williams, I. G. Kevrekidis, and C. W. Rowley, “A data-driven approximation of the Koopman operator: Extending dynamic mode decomposition,” *arXiv preprint arXiv:1408.4408* (2014).
- <sup>36</sup>H. D. Sherali and W. P. Adams, “A hierarchy of relaxations between the continuous and convex hull representations for zero-one programming problems,” *SIAM Journal on Discrete Mathematics* **3**, 411–20 (1990).
- <sup>37</sup>C. J. Albers, F. Critchley, and J. C. Gower, “Quadratic minimi-

- sation problems in statistics,” *Journal of Multivariate Analysis* **102**, 698–713 (2011).
- <sup>38</sup>C. W. Rowley, I. Mezić, S. Bagheri, P. Schlatter, and D. S. Henningson, “Spectral analysis of nonlinear flows,” *Journal of Fluid Mechanics* **641**, 115–127 (2009).
- <sup>39</sup>G.-R. Liu, *Meshfree methods: moving beyond the finite element method* (CRC press, 2010).
- <sup>40</sup>H. Wendland, “Meshless Galerkin methods using radial basis functions,” *Mathematics of Computation of the American Mathematical Society* **68**, 1521–1531 (1999).
- <sup>41</sup>G. E. Fasshauer, “Solving partial differential equations by collocation with radial basis functions,” in *Proceedings of Chamonix*, Vol. 1997 (Citeseer, 1996) pp. 1–8.
- <sup>42</sup>C. M. Bishop *et al.*, *Pattern recognition and machine learning*, Vol. 1 (springer New York, 2006).
- <sup>43</sup>I. Rypina, F. Beron-Vera, M. Brown, H. Kocak, M. Olascoaga, and I. Udovydchenkov, “On the Lagrangian dynamics of atmospheric zonal jets and the permeability of the stratospheric polar vortex,” arXiv preprint physics/0605155 (2006).
- <sup>44</sup>A. F. Shchepetkin and J. C. McWilliams, “The regional oceanic modeling system (ROMS): a split-explicit, free-surface, topography-following-coordinate oceanic model,” *Ocean Modelling* **9**, 347–404 (2005).
- <sup>45</sup>I. I. Rypina, A. R. Kirincich, R. Limeburner, and I. A. Udovydchenkov, “Eulerian and Lagrangian correspondence of high-frequency radar and surface drifter data: effects of radar resolution and flow components,” *Journal of Atmospheric and Oceanic Technology* **31**, 945–966 (2014).
- <sup>46</sup>A. C. Poje, T. M. Özgökmen, B. L. Lipphardt, B. K. Haus, E. H. Ryan, A. C. Haza, G. A. Jacobs, A. J. H. M. Reniers, M. J. Olascoaga, G. Novelli, A. Griffa, F. J. Beron-Vera, S. S. Chen, E. Coelho, P. J. Hogan, A. D. Kirwan, H. S. Huntley, and A. J. Mariano, “Submesoscale dispersion in the vicinity of the deep-water horizon spill,” *Proceedings of the National Academy of Sciences* **111**, 12693–12698 (2014).
- <sup>47</sup>I. I. Rypina, I. Kamenkovich, P. Berloff, and L. J. Pratt, “Eddy-induced particle dispersion in the near-surface North Atlantic,” *Journal of Physical Oceanography* **42**, 2206–2228 (2012).